Three-body Halos.
IV. Momentum Distributions after Fragmentation

E. Garrido, D.V. Fedorov and A.S. Jensen
Institute of Physics and Astronomy,
Aarhus University, DK-8000 Aarhus C, Denmark
(February 9, 2008)

Momentum distributions of particles from nuclear break-up of fast three-body halos are calculated incorporating effects of final state interactions. The same two-body interactions between the particles are used to calculate both the ground state structure and the final state of the reaction processes. The ground state wave function reproduces size and energy of the halo nucleus. First we give a general and detailed description of the method. Then we investigate the effect of final state interactions in neutron removal and core break-up reactions for one- and two-dimensional momentum distributions. We compute specifically core and neutron momentum distributions from ^{11}Li fragmentation and compare those with available experimental data. We conclude that ^{11}Li must have a neutron-core relative state containing a p-state admixture of 20%-30%. The fragmentation data also strongly suggest that ^{10}Li has an s-state at about 50 keV and a p-state around 500 keV.

PACS numbers: 25.60.+v, 21.45.+v, 21.60.Gx, 27.20.+n

I. INTRODUCTION

In the latest years a big effort has been made to investigate one of the most striking new features in nuclear physics: halo nuclei. They are weakly bound and spatially extended systems where one or two particles have a high probability of being at distances larger than the typical nuclear radius. General properties and the criteria for the ocurrence of nuclear halos have been discussed in [1–4] and a review of nuclear halos has recently been published [5].

The appearence of the halo structure in light nuclei along the neutron dripline [6] gives special interest to this region of nuclei. The most general properties of them are well described by few-body models, dividing the degrees of freedom into the approximately frozen (core) and the active (halo) degrees of freedom. In particular, special attention has been paid to Borromean systems consisting of three-body bound systems, where all the two-body subsystems are unbound [7,8]. The prototypes nuclear halos are ^{6}He (^{4}He+n+n) and ^{11}Li (^{9}Li+n+n), both thoroughly discussed in a general theoretical framework in [9].

The ability to produce secondary beams of halo nuclei opens the possibility of investigating their structure by measuring the momentum distribution of "particles" resulting from fragmentation reactions [10–16]. However one major problem in the interpretation of such measurements is the inherent mixture of effects from the original structure of the projectile and the reaction mechanism. Both should therefore be properly incorporated in model calculations.

The simplest picture used to describe this kind of fragmentation reactions is formulated in the sudden approximation, where one of the three particles in the projectile is instantaneously removed by the target, while the other two particles remain undisturbed. Clearly this can only be justified for reaction times much shorter than the characteristic time for the motion of the three particles in the system. Since the projectile is weakly bound this requirement is well fulfilled for any high-energy beam. The observed momentum distribution should then provide direct information about the three-body wave function. The validity of this model as a first description of the reaction has been discussed in the litterature, see for example [17–19].

The connection between the wave function and the momentum distributions is more complicated than originally anticipated when the early experiments were designed. It was found recently that momentum distributions are highly affected by the final state interaction (FSI) between the two particles remaining after the collision, especially when low-lying resonances are present [14,18,20]. This essential ingredient must then be incorporated into the model. The final state two-body interaction is at the same time determining the three-body structure of the projectile (halo nucleus), and therefore a consistent treatment of the initial and final states is needed to allow reliable interpretations of the experimental data.

This paper is number four in a series discussing the general properties of three-body halo systems. In the first of these [3] we discussed Borromean systems, in the second [4] we extended the discussion to general three-body systems and in the third [21] we discussed the effects of finite spin of the particles. In this paper we investigate

fragmentation reactions of Borromean projectiles by use of the sudden approximation. A brief report containing a few of the pertinent results for [11]Li is published [22]. Our main purpose is here to formulate a general procedure to incorporate the effects of final state two-body interactions. This two-body interaction is consistently included both in the final state wave function and in the description of the three-body projectile. We apply the method in detailed analyses of measured [11]Li fragmentation reactions. We thereby obtain essential information about the unbound [10]Li system.

The paper is organized as follows: The mathematical formalism is developed in Section 2, which to facilitate the understanding is divided in five subsections. The general numerical results are presented in Section 3, where we as illustration use parameters relevant for [11]Li fragmentation reactions. In Section 4 we perform realistic calculations for [11] Li and compare to experimental data. Finally, Section 5 contains a summary and the conclusions. Some of the mathematical definitions are collected in an appendix.

II. METHOD

To describe three-body halo fragmentation reactions we shall use the sudden approximation. We are then assuming a process where a high-energy three-body halo projectile instantaneously looses one of the particles without disturbing the remaining two. We also assume a light target and we shall therefore not consider Coulomb dissociation process, which then only contribute marginally .

We work in the center of mass system of the three-body projectile and denote by $\mathbf{k}$ and $\mathbf{q}$ the total and relative momentum of the two remaining particles in the final state. The transition matrix of the reaction in the sudden approximation is then given by

$$M(\mathbf{k}, \mathbf{q}) \propto \langle e^{i\mathbf{k}\cdot\mathbf{R}} e^{i\mathbf{q}\cdot\mathbf{r}} | \Psi \rangle \,, \tag{1}$$

where Ψ is the three-body wave function, $\mathbf{r}$ is the distance between the two reamining particles, and $\mathbf{R}$ is the distance between the center of mass of the two-body system and the removed particle.

This transition matrix describes the final state as a plane wave, which means that the interactions between the particles are neglected. In principle all of them should be included in the calculation, but under the experimental setup where one of the particles suddenly is removed, only the interaction between the two non-disturbed particles is present. To account for this final state two-body interaction the plane wave $e^{i\mathbf{q}\cdot\mathbf{r}}$ has to be replaced by the corresponding *distorted* two-body wave function $w(\mathbf{q}, \mathbf{r})$.

In the following subsections we describe how we construct the initial three-body halo wave function Ψ as well as the distorted two-body wave function $w(\mathbf{q}, \mathbf{r})$. Finally we compute the transtion matrix and the momentum distributions.

A. Initial Three-body Wave Function

We shall use the Jacobi coordinates, basically defined as the relative coordinates between two of the particles ($\mathbf{x}$) and between their center of mass and the third particle ($\mathbf{y}$). Three sets of Jacobi coordinates can be constructed and the precise definitions and the corresponding sets of hyperspherical coordinates (ρ, α, Ω_x, Ω_y) are given in the appendix. One of the three sets of hyperspherical coordinates is sufficient for a complete description of the system, but the subtle correlations are easier to describe by use of all three sets. The volume element is given by $\rho^5 d\Omega d\rho$, where $d\Omega = \sin^2\alpha \cos^2\alpha d\alpha d\Omega_x d\Omega_y$.

The total wave function Ψ_{JM} of the three-body system (with total spin J and projection M) is written as a sum of three components $\psi_{JM}^{(i)}$, which in turn for each ρ are expanded in a complete set of generalized angular functions $\Phi_{nJM}^{(i)}(\rho, \Omega_i)$

$$\Psi_{JM} = \sum_{i=1}^{3} \psi_{JM}^{(i)}(\mathbf{x}_i, \mathbf{y}_i) = \frac{1}{\rho^{5/2}} \sum_{n} f_n(\rho) \sum_{i=1}^{3} \Phi_{nJM}^{(i)}(\rho, \Omega_i) \,, \tag{2}$$

where the radial expansion coefficients $f_n(\rho)$ are component independent and $\rho^{-5/2}$ is the phase space factor.

These wave functions satisfy the three Faddeev equations [23,24]

$$(T - E)\psi_{JM}^{(i)} + V_{jk}(\psi_{JM}^{(i)} + \psi_{JM}^{(j)} + \psi_{JM}^{(k)}) = 0 \,, \tag{3}$$

where V_{jk} are the two-body interactions, E is the total energy, T is the kinetic energy operator and $\{i, j, k\}$ is a cyclic permutation of $\{1, 2, 3\}$.

The angular functions are now chosen for each ρ as the eigenfunctions of the angular part of the Faddeev equations:

$$\frac{\hbar^2}{2m}\frac{1}{\rho^2}\hat{\Lambda}^2\Phi^{(i)}_{nJM} + V_{jk}(\Phi^{(i)}_{nJM} + \Phi^{(j)}_{nJM} + \Phi^{(k)}_{nJM}) \equiv \frac{\hbar^2}{2m}\frac{1}{\rho^2}\lambda_n(\rho)\Phi^{(i)}_{nJM} , \tag{4}$$

where $\{i,j,k\}$ again is a cyclic permutation of $\{1,2,3\}$, m is an arbitrary normalization mass, and $\hat{\Lambda}^2$ is the ρ-independent part of the kinetic energy operator. The analytic expressions for $\hat{\Lambda}^2$ and the kinetic energy operator can for instance be found in [4].

The angular functions $\Phi^{(i)}_{nJM}(\rho,\Omega_i)$ are expanded in terms of the complete set of hyperspherical harmonics $\mathbf{Y}^{KL}_{\ell_x\ell_y}(\alpha_i,\Omega_{x_i},\Omega_{y_i})$, where the quantum number K usually is called the hypermoment, ℓ_x and ℓ_y are the orbital angular momenta associated with $\mathbf{x}$ and $\mathbf{y}$, and L is the coupling of these angular momenta. The result is

$$\Phi^{(i)}_{nJM}(\rho,\Omega_i) = \sum_{K\ell_x\ell_yLs_xS} C^{(i)}_{nK\ell_x\ell_yLs_xS}(\rho)\left[\mathbf{Y}^{KL}_{\ell_x\ell_y}(\alpha_i,\Omega_{x_i},\Omega_{y_i})\otimes\chi^{(i)}_{s_xs_yS}\right]^{JM} , \tag{5}$$

where C are expansion coefficients and $\chi^{(i)}_{s_xs_yS}$ is the three-body spin function. The spins of the two particles, connected by the $\mathbf{x}$ coordinate, couple to the spin s_x, which coupled to the spin s_y of the third particle results in the total spin S of the three-body system.

The radial expansion coefficients $f_n(\rho)$ are obtained from a coupled set of "radial" differential equations [4], i.e.

$$\left(-\frac{d^2}{d\rho^2} - \frac{2mE}{\hbar^2} + \frac{1}{\rho^2}\left(\lambda_n(\rho) + \frac{15}{4}\right)\right)f_n(\rho) + \sum_{n'}\left(-2P_{nn'}\frac{d}{d\rho} - Q_{nn'}\right)f_{n'}(\rho) = 0 , \tag{6}$$

where the functions P and Q are defined as angular integrals:

$$P_{nn'}(\rho) \equiv \sum_{i,j=1}^{3}\int d\Omega\Phi^{(i)*}_n(\rho,\Omega)\frac{\partial}{\partial\rho}\Phi^{(j)}_{n'}(\rho,\Omega) , \tag{7}$$

$$Q_{nn'}(\rho) \equiv \sum_{i,j=1}^{3}\int d\Omega\Phi^{(i)*}_n(\rho,\Omega)\frac{\partial^2}{\partial\rho^2}\Phi^{(j)}_{n'}(\rho,\Omega) . \tag{8}$$

Finally from eqs. (2) and (5) we obtain the expression of the three-body wave function

$$\Psi_{JM} = \frac{1}{\rho^{5/2}}\sum_n f_n(\rho)\sum_{i=1}^{3}\sum_{K\ell_x\ell_yLs_xS}C^{(i)}_{nK\ell_x\ell_yLs_xS}(\rho)\left[\mathbf{Y}^{KL}_{\ell_x\ell_y}(\alpha_i,\Omega_{x_i},\Omega_{y_i})\otimes\chi^{(i)}_{s_xs_yS}\right]^{JM} , \tag{9}$$

where the radial function $f_n(\rho)$ and the coefficients $C^{(i)}_{nK\ell_x\ell_yLs_xS}(\rho)$ must be computed numerically.

B. Final-state Two-body Wave Function

In the fragmentation reaction the target suddenly removes one of the particles from the projectile and the remaining interaction in the final state therefore acts between the two non-disturbed particles. Assuming that the two-body interaction does not mix two-body states with different spin s_x and relative orbital angular momentum ℓ_x, we can expand the two-body wave function in partial waves, see [25], as

$$w^{s_x\sigma_x}(\mathbf{k}_x,\mathbf{x}) = \sqrt{\frac{2}{\pi}}\frac{1}{k_x x}\sum_{j_x\ell_x m_x}u^{j_x}_{\ell_x s_x}(k_x,x)\mathcal{Y}^{m_x^*}_{j_x\ell_x s_x}(\Omega_x)$$

$$\times\sum_{m_{\ell_x}=-\ell_x}^{\ell_x}\langle\ell_x m_{\ell_x}s_x\sigma_x|j_x m_x\rangle i^{\ell_x}Y_{\ell_x m_{\ell_x}}(\Omega_{k_x}) , \tag{10}$$

where σ_x is the spin projection of s_x, u is the radial and $\mathcal{Y}$ the angular distorted wave function. The angles Ω_x and Ω_{k_x} define the direction of $\mathbf{x}$ and $\mathbf{k}_x$. These assumptions are usually strictly valid. The only exception arises from

the tensor interaction and even then the resulting mixing is often very small and therefore insignificant in the present context.

The two-body space and momentum coordinates $\mathbf{x}$ and $\mathbf{k}_x$ are defined consistently with the Jacobi coordinates introduced in the three-body wave function (see appendix)

$$\mathbf{x} = \sqrt{\frac{\mu}{m}} \mathbf{r} , \qquad \mathbf{k}_x = \sqrt{\frac{m}{\mu}} \mathbf{p}_r , \tag{11}$$

where $\mathbf{r}$ is the relative spatial coordinate and $\mathbf{p}_r$ the relative momentum. The mass m is the arbitrary normalization mass and μ is the reduced mass of the two-body system.

The radial functions $u_{\ell_x s_x}^{j_x}(k_x, x)$ are obtained numerically by solving the Schrödinger equation with the appropriate two-body potential $\hat{V}(\mathbf{x})$

$$\frac{\partial^2}{\partial x^2} u_{\ell_x s_x}^{j_x}(k_x, x) + \left(k_x^2 - \frac{2m}{\hbar^2} V_{\ell_x s_x}^{j_x}(x) - \frac{\ell_x(\ell_x + 1)}{x^2} \right) u_{\ell_x s_x}^{j_x}(k_x, x) = 0 , \tag{12}$$

where

$$V_{\ell_x s_x}^{j_x}(x) = \int d\Omega_x \mathcal{Y}_{j_x \ell_x s_x}^{m_x *}(\Omega_x) \hat{V}(\mathbf{x}) \mathcal{Y}_{j_x \ell_x s_x}^{m_x}(\Omega_x) . \tag{13}$$

When the interaction between the two particles is neglected the solution of eq.(12) is $(k_x x) j_{\ell_x}(k_x x)$, and the expansion in eq.(10) reduces to the usual expansion of a plane wave in terms of spherical Bessel functions j_ℓ.

C. Transition Matrix

To compute the transition matrix in eq.(1) it is convenient to rewrite the three-body wave function in eq.(9) in terms of the set of Jacobi coordinates where $\mathbf{x}$ is related to the two particles remaining after the fragmentation. This means that all three Faddeev components in eq.(2) have to be expressed in terms of the chosen set of Jacobi coordinates. The three-body wave function can then be written

$$\Psi_{JM}(\mathbf{x}, \mathbf{y}) = \frac{1}{\rho^{5/2}} \sum_n f_n(\rho) \sum_{K\ell_x\ell_y Ls_x S} \tilde{C}_{nK\ell_x\ell_y Ls_x S}(\rho) \left[\mathbf{Y}_{\ell_x\ell_y}^{KL}(\alpha, \Omega_x, \Omega_y) \otimes \chi_{s_x s_y S} \right]^{JM} , \tag{14}$$

where $\tilde{C}_{nK\ell_x\ell_y Ls_x S}(\rho)$ are the coefficients of the expansion after the transformation.

The calculation of the transition matrix involves the overlap of eq.(14) and the function $e^{i\mathbf{k}_y \cdot \mathbf{y}} w^{s_x \sigma_x}(\mathbf{k}_x, \mathbf{x})$ (see eqs.(1) and (10) and note that $\mathbf{k} \cdot \mathbf{R} = \mathbf{k}_y \cdot \mathbf{y}$, where $\mathbf{k}_y$ is the momentum related to $\mathbf{y}$). After integrating analytically over Ω_x and Ω_y we get for each λ_n the following expression for the transition matrix:

$$M_{s_x \sigma_x s_y \sigma_y}^{JM}(\mathbf{k}_x, \mathbf{k}_y) \propto \frac{2}{\pi} \sum_{\ell_x m_{\ell_x} \ell_y m_{\ell_y} \ j_x LS} I_{\ell_x s_x j_x}^{\ell_y LS}(\kappa, \alpha_\kappa) Y_{\ell_x m_{\ell_x}}(\Omega_{k_x}) Y_{\ell_y m_{\ell_y}}(\Omega_{k_y})$$

$$\times \sum_{m_x j_y m_y} (-1)^{J+2S-2M+\ell_y+s_y-s_x-\ell_x} \hat{j}_x^2 \hat{j}_y^2 \hat{J}\hat{L}\hat{S} \begin{pmatrix} J & j_x & j_y \\ M & -m_x & -m_y \end{pmatrix}$$

$$\times \begin{pmatrix} j_y & \ell_y & s_y \\ -m_y & m_{\ell_y} & \sigma_y \end{pmatrix} \begin{pmatrix} j_x & \ell_x & s_x \\ -m_x & m_{\ell_x} & \sigma_x \end{pmatrix} \begin{Bmatrix} J & j_x & j_y \\ L & \ell_x & \ell_y \\ S & s_x & s_y \end{Bmatrix} , \tag{15}$$

where $\hat{a} \equiv \sqrt{2a+1}$, σ_y is the projection of s_y, ( ) and { } are the usual 3J and 9J symbols, see [26]. We have introduced the hyperspherical coordinates in momentum space $\kappa = \sqrt{k_x^2 + k_y^2}$, $\alpha_\kappa = \arctan(k_x/k_y)$ and the function $I_{\ell_x s_x j_x}^{\ell_y LS}(\kappa, \alpha_\kappa)$ is given by

$$I_{\ell_x s_x j_x}^{\ell_y LS}(\kappa, \alpha_\kappa) = i^{\ell_x+\ell_y} \sum_K N_K^{\ell_x \ell_y} \int_0^\infty \rho^{5/2} d\rho f(\rho) \tilde{C}_{nK\ell_x\ell_y Ls_x S}(\rho) \tag{16}$$

$$\times \left[\int_0^{\pi/2} d\alpha (\sin\alpha)^{\ell_x+2} (\cos\alpha)^{\ell_y+2} P_\nu^{\ell_x+\frac{1}{2},\ell_y+\frac{1}{2}}(\cos(2\alpha)) j_{\ell_y}(k_y y) \frac{1}{k_x x} u_{\ell_x s_x}^{j_x}(k_x, x) \right] ,$$

4

where $\nu = (K - \ell_x - \ell_y)/2$, $P_\nu^{\ell_x+\frac{1}{2},\ell_y+\frac{1}{2}}$ is a Jacobi polynomial and

$$N_K^{\ell_x \ell_y} = \left[\frac{\nu!(\nu + \ell_x + \ell_y + 1)!2(K+2)}{\Gamma(\nu + \ell_x + \frac{3}{2})\Gamma(\nu + \ell_y + \frac{3}{2})} \right]^{1/2} . \tag{17}$$

When the interaction between the two particles in the final state is ignored the integral over α in eq.(16) can be carried out analytically, i.e.

$$\int_0^{\pi/2} d\alpha (\sin\alpha)^{\ell_x+2}(\cos\alpha)^{\ell_y+2} P_\nu^{\ell_x+\frac{1}{2},\ell_y+\frac{1}{2}}\left(\cos(2\alpha)\right) j_{\ell_y}(k_y y) j_{\ell_x}(k_x x) =$$

$$\times (-1)^\nu \frac{\pi}{2}(\sin\alpha_\kappa)^{\ell_x}(\cos\alpha_\kappa)^{\ell_y} P_\nu^{\ell_x+\frac{1}{2}\ell_y+\frac{1}{2}}\left(\cos(2\alpha_\kappa)\right) \frac{J_{K+2}(\kappa\rho)}{(\kappa\rho)^2} \tag{18}$$

D. Momentum Distributions

The cross section or momentum distribution is now obtained by squaring the transition matrix and subsequently averaging over initial states and summing over final states:

$$\frac{d^6\sigma}{d\mathbf{k}_x d\mathbf{k}_y} \propto \sum_M \sum_{s_x \sigma_x s_y \sigma_y} |M_{s_x \sigma_x s_y \sigma_y}^{JM}(\mathbf{k}_x, \mathbf{k}_y)|^2 . \tag{19}$$

The volume element $d\mathbf{k}_x d\mathbf{k}_y$ is written

$$d\mathbf{k}_x d\mathbf{k}_y = k_x^\perp dk_x^\perp dk_x^\parallel d\varphi_{k_x} k_y^2 dk_y d\Omega_{k_y} , \tag{20}$$

where $k_x^\perp = k_x \sin\theta_{k_x}$, $k_x^\parallel = k_x \cos\theta_{k_x}$, and $(\theta_{k_x}, \varphi_{k_x})$ are the polar and azimuthal angles of the vector $\mathbf{k}_x$. The differential cross section in eq.(19) should be integrated over all unobserved variables.

Substituting eq.(15) into (19) we obtain, after analytical integration over Ω_{k_y} and φ_{k_x}, the following expression for the three-dimensional differential cross section or momentum distribution:

$$\frac{d^3\sigma}{dk_y dk_x^\perp dk_x^\parallel} \propto k_y^2 k_x^\perp \frac{2}{\pi^2} \sum_{j_x \ell_x s_x} \sum_{LSL'S'} \sum_{\ell_y j_y} \hat{j}_x^2 \hat{j}_y^2 \hat{L}\hat{L}'\hat{S}\hat{S}' I_{\ell_x s_x j_x}^{\ell_y LS}(\kappa, \alpha_\kappa) I_{\ell_x s_x j_x}^{\ell_y L'S'}(\kappa, \alpha_\kappa)$$

$$\times \left\{ \begin{matrix} J & j_x & j_y \\ L & \ell_x & \ell_y \\ S & s_x & s_y \end{matrix} \right\} \left\{ \begin{matrix} J & j_x & j_y \\ L' & \ell_x & \ell_y \\ S' & s_x & s_y \end{matrix} \right\} . \tag{21}$$

By integrating numerically over k_y and $k_x^\perp$, we get the one-dimensional relative momentum $(k_x^\parallel)$ distribution of the remaining particles. By integrating over k_y and $k_x^\parallel$, we get instead the two-dimensional relative momentum $(k_x^\perp)$ distribution.

It should be noted that we have not specified any coordinate system and the axes $\mathbf{x}$, $\mathbf{y}$, and $\mathbf{z}$ are therefore completely arbitrary. Thus, in the sudden approximation the longitudinal and transverse momentum distributions are identical.

E. Transformation to the Center of Mass of the Three-body System

Comparison with the measured momentum distributions requires transformation to the center of mass system of the projectile. To do this we construct the momentum $\mathbf{p}$ of one of the particles in the final state relative to the center of mass of the projectile as a linear combination of $\mathbf{k}_x$ and $\mathbf{k}_y$

$$\mathbf{p} = a_i \mathbf{k}_x + b_i \mathbf{k}_y . \tag{22}$$

If the Jacobi coordinate $\mathbf{x}$ refers to particles 1 and 2, then a and b take the set of values (see eqs.(A4) and (A5))

$$a_1 = -\left(\frac{1}{m} \frac{m_1 m_2}{m_1 + m_2} \right)^{1/2} , \qquad b_1 = \frac{m_1}{m_1 + m_2} \left(\frac{1}{m} \frac{(m_1 + m_2)m_3}{m_1 + m_2 + m_3} \right)^{1/2} , \tag{23}$$

5

$$a_2 = \left(\frac{1}{m} \frac{m_1 m_2}{m_1 + m_2} \right)^{1/2} , \qquad b_2 = \frac{m_2}{m_1 + m_2} \left(\frac{1}{m} \frac{(m_1 + m_2) m_3}{m_1 + m_2 + m_3} \right)^{1/2} , \tag{24}$$

when we compute the momentum distributions of particle 1 and 2, respectively.

Using the momentum $\mathbf{p}$ of one of the particles as the variable instead of $\mathbf{k}_x$ we obtain the relation

$$\frac{d^6 \sigma}{d\mathbf{p} d\mathbf{k}_y} = \frac{1}{a_i^3} \frac{d^6 \sigma}{d\mathbf{k}_x d\mathbf{k}_y} \propto \frac{1}{a_i^3} \sum_M \sum_{s_x \sigma_x s_y \sigma_y} |M_{s_x \sigma_x s_y \sigma_y}^{JM}(\mathbf{k}_x, \mathbf{k}_y)|^2 , \tag{25}$$

where a_i^3 arises from the Jacobi determinant for the transformation.

As before we must integrate eq.(25) over the unobserved quantities, i.e. $\mathbf{k}_y$ and some of the components of $\mathbf{p}$. It is then convenient to use both the initial (arbitrary) coordinate system and a rotated system where the z-axis is along $\mathbf{p}$. The volume element is then written as

$$d\mathbf{p} d\mathbf{k}_y = p^\perp dp^\perp dp^\parallel d\varphi_p k_y^2 dk_y d\Omega'_{k_y} , \tag{26}$$

where $p^\perp = p \sin \theta_p$, $p^\parallel = p \cos \theta_p$, (θ_p, φ_p) define the direction of $\mathbf{p}$ in the initial coordinate system and the angles $\Omega'_{k_y} = (\theta'_{k_y}, \varphi'_{k_y})$ give the direction of $\mathbf{k}_y$ in the rotated system.

We express the transition matrix in eq.(15) as a function of $\mathbf{p}$ referred to the initial system and $\mathbf{k}_y$ referred to the rotated system. Then we need the relations

$$Y_{\ell m}(\theta_{k_y}, \varphi_{k_y}) = \sum_{m'} \mathcal{D}_{mm'}^{\ell*}(\varphi_p, \theta_p, 0) Y_{\ell m'}(\theta'_{k_y}, \varphi'_{k_y}) , \tag{27}$$

$$Y_{\ell m}(\theta_{k_x}, \varphi_{k_x}) = \sum_{m'} \mathcal{D}_{mm'}^{\ell*}(\varphi_p, \theta_p, 0) Y_{\ell m'}(\theta'_{k_x}, \varphi'_{k_x}) , \tag{28}$$

where $\mathcal{D}(\varphi_p, \theta_p, 0)$ is the rotation matrix (the $\mathcal{D}$-functions) defined in [26], and the angles $(\theta'_{k_x}, \varphi'_{k_x})$ defining the direction of $\mathbf{k}_x$ in the rotated system are given by

$$\cos \theta'_{k_x} = \frac{p - b_i k_y \cos \theta'_{k_y}}{a_i k_x} , \tag{29}$$

$$\varphi'_{k_x} = \begin{cases} \varphi'_{k_y} & \text{if } a_i/b_i < 0 \\ \varphi'_{k_y} + \pi & \text{if } a_i/b_i > 0 \end{cases} \tag{30}$$

Finally, we need to express κ and α_κ in terms of the new variables p, k_y and θ'_{k_y}, i.e.

$$\kappa^2 = \frac{1}{a_i^2} \left(p^2 + b_i^2 k_y^2 - 2 b_i p k_y \cos \theta'_{k_y} \right) + k_y^2 , \tag{31}$$

$$\tan \alpha_\kappa = \frac{k_x}{k_y} = \frac{(p^2 + b_i^2 k_y^2 - 2 b_i p k_y \cos \theta'_{k_y})^{1/2}}{|a_i| k_y} , \qquad 0 \leq \alpha_\kappa \leq \frac{\pi}{2} . \tag{32}$$

The numerically obtained function $I_{\ell_x s_x j_x}^{\ell_y LS}(\kappa, \alpha_\kappa)$ in eq.(15) depends on θ'_{k_y} and only the integrations over φ_p and φ'_{k_y} in eq.(25) can be done analytically. We then obtain the four-dimensional differential cross section or momentum distribution relative to the center of mass of the projectile

$$\frac{d^4 \sigma}{dk_y d\theta'_{k_y} dp^\perp dp^\parallel} \propto k_y^2 p^\perp \frac{1}{a_i^3 \pi^2} \sin \theta'_{k_y} \sum_{\ell_x s_x j_x LS} \sum_{\ell'_x j'_x L'S'} \sum_{\ell_y j_y \ell'_y j'_y} (-1)^{s_y - s_x + j'_y + j_y + J}$$

$$\times \hat{j}_x^2 \hat{j}_x'^2 \hat{j}_y^2 \hat{j}_y'^2 \hat{\ell}_x \hat{\ell}_x' \hat{\ell}_y \hat{\ell}_y' \hat{L} \hat{L}' \hat{S} \hat{S}' I_{\ell_x s_x j_x}^{\ell_y LS}(\kappa, \alpha_\kappa) I_{\ell'_x s_x j'_x}^{\ell'_y L'S'}(\kappa, \alpha_\kappa) \begin{Bmatrix} J & j_x & j_y \\ L & \ell_x & \ell_y \\ S & s_x & s_y \end{Bmatrix}$$

$$\times \begin{Bmatrix} J & j'_x & j'_y \\ L' & \ell'_x & \ell'_y \\ S' & s_x & s_y \end{Bmatrix} \sum_{L_x} \hat{L}_x^2 \begin{pmatrix} \ell_x & \ell'_x & L_x \\ 0 & 0 & 0 \end{pmatrix} \begin{pmatrix} \ell_y & \ell'_y & L_x \\ 0 & 0 & 0 \end{pmatrix} \begin{Bmatrix} j_y & j'_y & L_x \\ \ell'_y & \ell_y & s_y \end{Bmatrix}$$

$$\times \begin{Bmatrix} j_x & j'_x & L_x \\ \ell'_x & \ell_x & s_x \end{Bmatrix} \begin{Bmatrix} j_x & j'_x & L_x \\ j'_y & j_y & J \end{Bmatrix} \sum_{N_x} (-1)^{N_x} P_{L_x}^{N_x}(\cos \theta'_{k_x}) P_{L_x}^{-N_x}(\cos \theta'_{k_y}) , \tag{33}$$

6

where we assumed that $a_i < 0$. When $a_i > 0$, the summation over N_x should include an extra factor $(-1)^{N_x}$.

Three integrations must be done numerically in order to get the one-dimensional $(p^{\parallel})$ and two-dimensional $(p^{\perp})$ momentum distributions of one of the particles in the final state relative to the center of mass of the projectile.

If we assume that one of the particles in the final state, say particle 1, has infinite mass, then the momentum distribution of particle 2 relative to the three-body center of mass should coincide with the momentum distribution relative to particle 1. In other words, eq.(21) should be recovered by integrating eq.(33) over θ'_{k_y}. Then $b_i = 0$ (see eq.(24)), $\mathbf{p} = a_i \mathbf{k}_x$ and therefore $\theta'_{k_x} = 0$ and $P_{L_x}^{N_x}(1) = \delta_{N_x,0}$. Now κ and α_κ are independent of θ'_{k_y} (eqs.(31) and (32)) and the integration over θ'_{k_y} can easily be done analytically leading directly to eq.(21).

III. NUMERICAL RESULTS

In this section we apply the method to the fragmentation of two-neutron halo nuclei (core+n+n). Two different kinds of processes will be considered: neutron removal and core break-up reactions. In the first case one of the neutrons is removed by the target, and the neutron-core interaction in the final state must be considered. In the second case, where the core is violently removed from the projectile, the neutron-neutron interaction is involved in the final state.

We take parameters corresponding to ^{11}Li in our examples. We first specify the two-body potentials used in the calculation. We then investigate the momentum distributions and how they are affected by final state interactions and the structure of the projectile.

A. Two-body Potentials

Loosely bound systems are mainly sensitive to the low-energy properties of the potentials. We shall therefore use relatively simple potentials reproducing the available low-energy scattering data and still allowing extensive three-body calculations.

For the neutron-neutron interaction in the singlet s-wave we use the gaussian potential introduced in ref. [8]. The extension to the triplet p-wave is made by including spin-spin, spin-orbit, and tensor terms. The neutron-neutron potential has then the form

$$V_{nn} = \left(V_c + V_{ss} \mathbf{s}_{n1} \cdot \mathbf{s}_{n2} + V_T \hat{S}_{12} + V_{so} \mathbf{l}_{nn} \cdot \mathbf{s}_{nn} \right) \exp\left[-(r/b_{nn})^2 \right] \; , \tag{34}$$

where $\mathbf{s}_{n1}$ and $\mathbf{s}_{n2}$ are the spins of the two neutrons, $\mathbf{s}_{nn} = \mathbf{s}_{n1} + \mathbf{s}_{n2}$, $\mathbf{l}_{nn}$ is the relative neutron-neutron orbital angular momentum and $\hat{S}_{12}$ is the ususal tensor operator.

The strength parameters V_c, V_{ss}, V_T, and V_{so}, and the range parameter b_{nn} are adjusted to reproduce the following scattering lengths a and the s-wave effective range r_e [27]:

$$a(^1S_0) = 18.8 \text{ fm} \quad , r_e(^1S_0) = 2.76 \text{ fm} \; , \tag{35}$$

$$a(^3P_0) = 3.6 \text{ fm} \quad , a(^3P_1) = -2.0 \text{ fm} \quad , a(^3P_2) = 0.30 \text{ fm} \; . \tag{36}$$

We then obtain values for the parameters of the potential

$$V_c = 2.92 \text{ MeV} \quad , \quad V_{ss} = 45.22 \text{ MeV} \; , \tag{37}$$

$$V_T = 26.85 \text{ MeV} \quad , V_{so} = -12.08 \text{ MeV} \; , \tag{38}$$

$$b_{nn} = 1.8 \text{ fm} \; . \tag{39}$$

For the neutron-core potential we also assume a gaussian shape and we use the parametrization

$$V_{nc}^{(s)} = V_s (1 + \gamma_s \mathbf{s}_c \cdot \mathbf{s}_n) \exp\left[-(r/b_{nc})^2 \right], \tag{40}$$

$$V_{nc}^{(l)} = (V_l + V_{so}^{(l)} \mathbf{l}_{nc} \cdot \mathbf{s}_{nc}) \exp\left[-(r/b_{nc})^2 \right] \; , \tag{41}$$

where $\mathbf{s}_c$ and $\mathbf{s}_n$ are the spins of the core and the neutron, $\mathbf{s}_{nc} = \mathbf{s}_c + \mathbf{s}_n$ and $\mathbf{l}_{nc}$ is the relative neutron-core orbital angular momentum. This choice is convenient when we adjust the all-decisive energy positions of the virtual states and the resonances in the neutron-core subsystem. The spin splitting term $\mathbf{s}_c \cdot \mathbf{s}_n$ is for simplicity only introduced in the s-state, but it could as well be included for other partial waves.
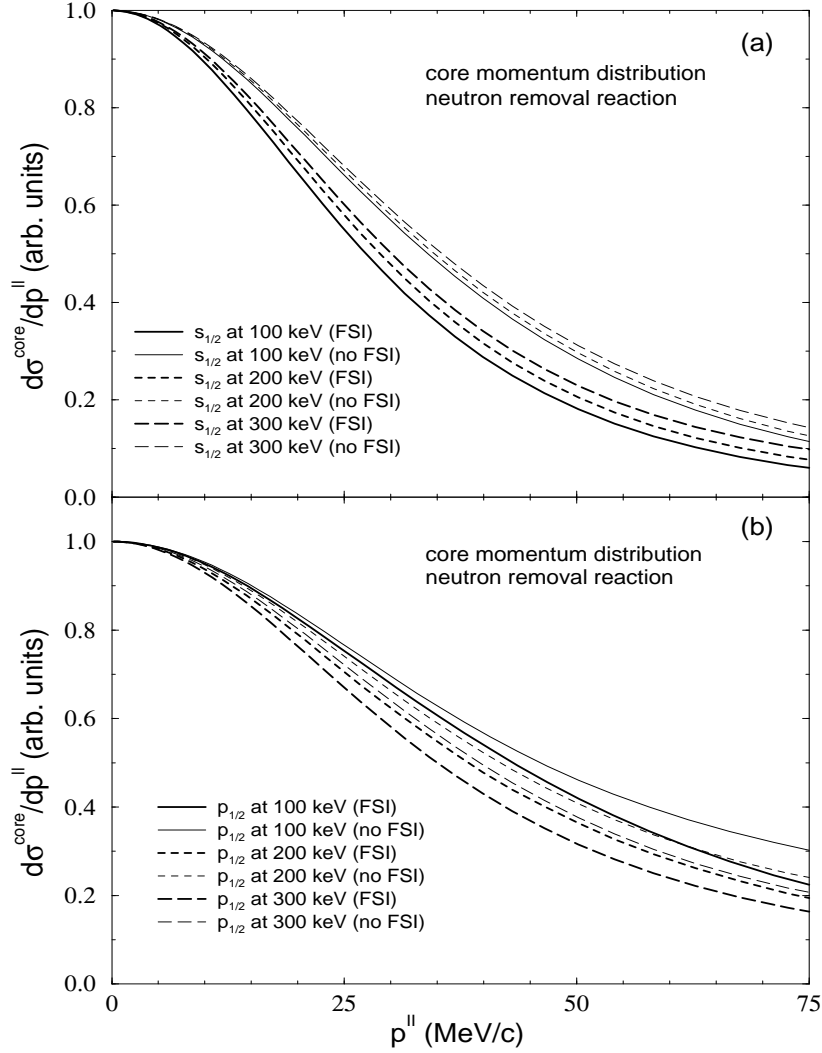
FIG. 1. One-dimensional core momentum distribution for a neutron removal process in ^{11}Li fragmentation. Thin curves correspond to calculations without FSI, while FSI are included for the thick curves. In the upper part the virtual $s_{1/2}$-state is placed at 100 keV (solid curve), 200 keV (short-dashed curve), and 300 keV (long-dashed curve), respectively. In the lower part the $p_{1/2}$-resonance is placed at 100 keV (solid curve), 200 keV (short-dashed curve) and 300 keV (long-dashed curve), respectively. The momentum of the core is referred to the center of mass of the ^{11}Li projectile. The ^{11}Li spin is assumed to be zero.

$E_{s_{1/2}}$ (keV)	$E_{p_{1/2}}$ (keV)	V_s (MeV)	$V_{l=1}$ (MeV)	V_{so} (MeV)	b_{nc} (fm)	s-wave (%)	p-wave (%)
100	>5000	−7.80	−4.5	10.80	2.55	97	3
200	1700	−7.14	−4.5	30.87	2.55	84	16
300	860	−6.64	−4.5	33.60	2.55	73	27
810	300	−4.94	−4.5	36.42	2.55	49	51
1280	200	−3.85	−4.5	37.03	2.55	36	64
2600	100	−1.46	−4.5	37.67	2.55	22	78

TABLE I. Energy positions of the virtual $s_{1/2}$-state and the $p_{1/2}$-resonance in the neutron-^{9}Li subsystem (first and second column) and the parameters of the neutron-core potential for each case. The last two columns give the s- and p-wave content in the neutron-^{9}Li subsystem in the three-body wave function of ^{11}Li.

B. Momentum Distributions for Spin Zero Core

We analyze the general properties of momentum distributions and the effects of final state interactions by taking ^{11}Li as an example. We include s- and p-waves in the Faddeev components and neglect all higher orbital angular momenta, since their contributions are expected to be exceedingly small.

We first consider the simpler case where the spin of the ^{9}Li-core is assumed to be zero. The spin quantum numbers of ^{10}Li and ^{11}Li are correspondingly 1/2 and 0. The range parameter b_{nc} in eqs. (40) and (41) is assumed to be 2.55 fm [8]. The strength parameter V_s is used to modify the position of the virtual $s_{1/2}$-state in ^{10}Li. The parameter $V_{l=1}$ is chosen as -4.5 MeV and the spin-orbit parameter V_{so} must be large to reproduce the experimental binding energy (295 ± 35 keV [28]) and root mean square radius (3.1 ± 0.3 fm [29]) of ^{11}Li. With this choice of the parameters we have a simple structure for the three-body system, where only the positions of the virtual $s_{1/2}$-state and the $p_{1/2}$-resonance in ^{10}Li are relevant. In particular, then a $p_{3/2}$-resonance appears at a very large energy. We can now investigate how the momentum distributions are influenced by final state interactions for different structures of the neutron-core subsystem.

Comparing the cases of low-lying virtual s-states and low-lying p-resonances are of special interest. Six different situations are considered: The virtual $s_{1/2}$-state in ^{10}Li is at 100, 200, and 300 keV, and the $p_{1/2}$-resonance is at 100, 200, and 300 keV. Because of the requirement of reproducing the experimental binding energy and rms radius in ^{11}Li both the virtual $s_{1/2}$-state and the $p_{1/2}$-resonance can not simultaneously be at a low energy [21]. In table I we show the values of the parameters used in the neutron-core interaction as well as the resulting s- and p-wave content in the neutron-core subsystem of the total three-body wave function.

In fig.1 we show the one-dimensional core momentum distribution for a neutron removal reaction measured in the center of mass of the three-body projectile. To make the comparison easier all the curves have been scaled to the same maximum. The thin curves are the calculations without final state interactions while the thick curves are obtained with final state interactions. In the upper part of the figure the virtual $s_{1/2}$-state has been placed at 100 keV (solid curve), 200 keV (short-dashed curve) and 300 keV (long-dashed curve), and in the lower part the $p_{1/2}$-resonance energy is at 100 keV (solid curve), 200 keV (short-dashed curve) and 300 keV (long-dashed curve). The full width at half maximum (FWHM) for the momentum distributions in the figure are given in the second and third columns of table II.

From fig.1 and table II we observe the two important features. First, for a given neutron-^{9}Li structure final state interactions always make the momentum distributions narrower. The change is not drastic, due to the large mass of the core, but it is still important. The largest effects appear for low-lying virtual $s_{1/2}$-states, where the FWHM decreases by 15-19%. For low-lying p-resonances the FWHM decreases by less than 10%. Thus, the larger the s-wave content in the neutron-core subsystem, the larger the effect of final state interactions.

Secondly, the width of the momentum distributions increases from 55 MeV/c, when the virtual $s_{1/2}$-state is at 100 keV, to 87 MeV/c, when the $p_{1/2}$-resonance is at 100 keV. The corresponding numbers without final state interactions are 68 MeV/c and 92 MeV/c. Comparison with the experimental value in table II strongly suggests a low-lying virtual s-state in ^{10}Li. The corresponding s-wave content decreases from 97% for the narrowest to only 22% for the broadest distribution. Thus the larger the s-wave content in the initial neutron-core subsystem of ^{11}Li, the narrower the momentum distribution.

Energy	core		neutron		
(keV)	no FSI	FSI$^{(n-c)}$	no FSI	FSI$^{(n-c)}$	FSI$^{(n-n)}$
$E_{s_{1/2}} = 100$	68	55	51	28	39
$E_{s_{1/2}} = 200$	69	58	53	34	40
$E_{s_{1/2}} = 300$	71	60	55	40	41
$E_{p_{1/2}} = 300$	79	70	68	48	46
$E_{p_{1/2}} = 200$	84	77	77	43	48
$E_{p_{1/2}} = 100$	92	87	94	31	55
Experimental		$49 \pm 3^{(a)}$		$25\text{-}35^{(b)}$	$43 \pm 3^{(c)}$

TABLE II. Full width at half maximum in MeV/c of the one-dimensional core and neutron momentum distributions from ^{11}Li fragmentation for different positions of the virtual $s_{1/2}$-state and the $p_{1/2}$-resonance. Columns 2 and 3 refer to core momentum distributions, while 4 to 6 refer to neutron momentum distributions. The label (n-c) indicates that final state interactions between ^{9}Li and the neutron have been included in this neutron removal process. The label (n-n) indicates that final state interactions between the two neutrons have been included (core break-up) [a] Data from [16]. [b] See, for instance, [11]. [c] Data from [15].

These two facts can be explained by the effects of the centrifugal barrier. A high p-wave content in the neutron-core subsystem increases the importance of the centrifugal barrier, see eq.(12). Consequently the effects of distortion from the short-range potentials is smaller for p-waves than for s-waves. Therefore the effects of final state interactions decreases when the p-wave content increases. Furthermore, the probability for the neutron to be outside the range of the two-body potential drastically decreases for p-waves [1,3]. This decreases the spatial extension of the initial system when the p-wave content increases, and the momentum distribution is then broader.
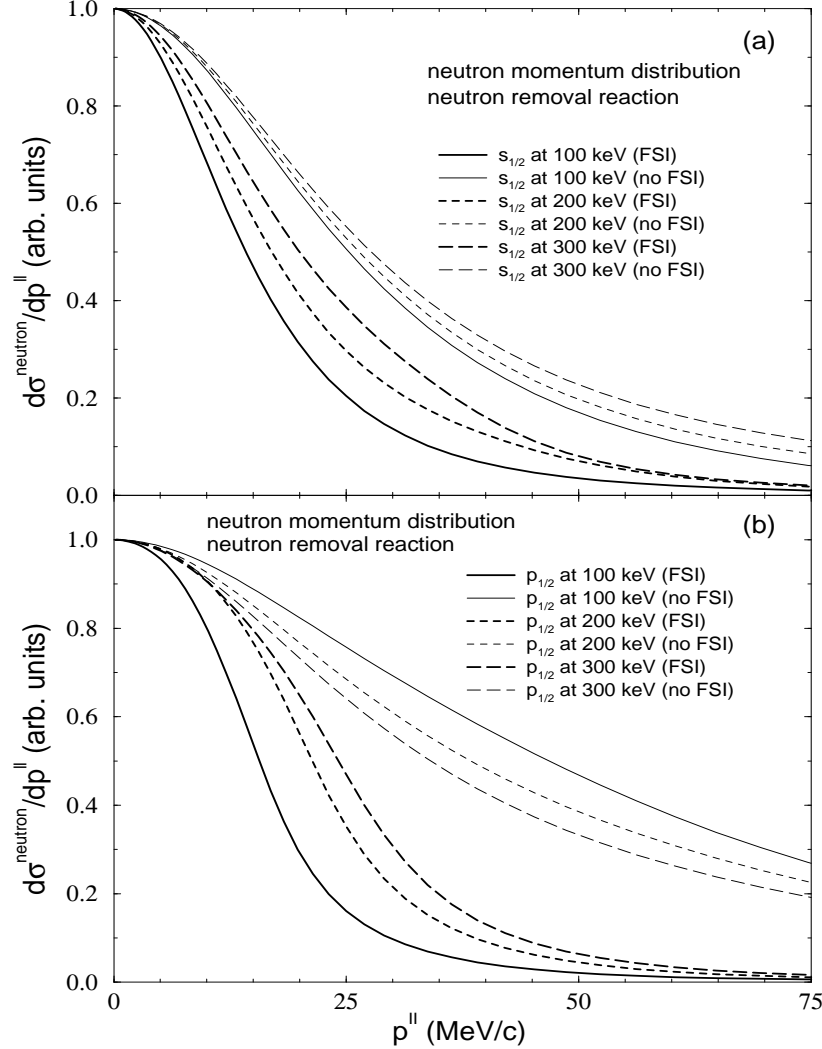
FIG. 2. The same as fig.1 for one-dimensional neutron momentum distributions.

In fig.2 we show the one-dimensional neutron momentum distributions for a neutron removal process. The notation to distinguish the curves is the same as in fig.1. The FWHM for these distributions are shown in the fourth and fifth columns of table II. Let us focus first on the momentum distributions without final state interactions (thin curves). As in fig.1 we observe that a higher s-wave content in the neutron-^{9}Li subsystem decreases the widths of the momentum distributions. The FWHM decreases from 94 MeV/c to 51 MeV/c when the s-wave content increases from 22% to 97%.

When final state interactions are included in the calculations (thick curves), the change in the neutron momentum distributions is much more significant than for core momentum distributions. For low-lying virtual $s_{1/2}$-states (upper part of fig.2) the width of the distribution decreases for a virtual state at 100 keV by as much as 45% due to final state interactions. We still observe that the lower the virtual $s_{1/2}$-state (high s-wave content in the neutron-core subsystem) the narrower the momentum distribution. For low-lying $p_{1/2}$-resonances in ^{10}Li (lower part of fig.2) we also observe a drastic modification of the neutron momentum distributions due to final state interactions. However,

we now see that the lower the $p_{1/2}$-resonance (higher p-wave content) the narrower the momentum distribution. This result seems to contradict our experience from the core momentum distribution where the presence of the centrifugal barrier was decisive. But the effect of final state interactions on the much lighter neutron in a low-lying p-resonance is apparently much larger than the simultaneous broadening due to the centrifugal barrier.

We can try to estimate the peak position of the p-wave contribution to the momentum distribution. The relative momentum ($\mathbf{p}_r$) between the neutron and the core in the final state preferably takes the value $\sqrt{2\mu E_{res}/\hbar^2}$, where E_{res} is the energy of the resonance and μ is the reduced mass of the two-body system. The momentum of the neutron relative to the center of mass of the projectile is very close to $\mathbf{k}_x$, since the constant b_i in eq.(22) is close to zero due to the large mass of the core. Then the neutron momentum distributions in fig.2 would be concentrated around the relative momentum $\mathbf{p}_r = \sqrt{\mu/m}\mathbf{k}_x$, see eq.(11). If the resonance energy is low, the final state interactions would try to create a narrow momentum distribution. This argument is valid for both low-lying virtual $s_{1/2}$-states and low-lying $p_{1/2}$-resonances. Thus, we can obtain a narrow neutron momentum distribution with FWHM compatible with the experimental value in table II both with low-lying $s_{1/2}$ and $p_{1/2}$-states.

For two-dimensional neutron and core momentum distributions in a neutron removal process we obtain conclusions similar to those extracted from figs.1 and 2. As a general rule we can say that momentum distributions are narrower and more affected by final state interactions when a low-lying virtual s-state is present in the neutron-core subsystem (high s-wave content) than with a low-lying p-resonance (low s-wave content). As for the one-dimensional distributions the neutron momentum distributions influenced by the final state interactions do not follow this rule. We can also get a narrow momentum distribution with a low-lying $p_{1/2}$-resonance in ^{10}Li.
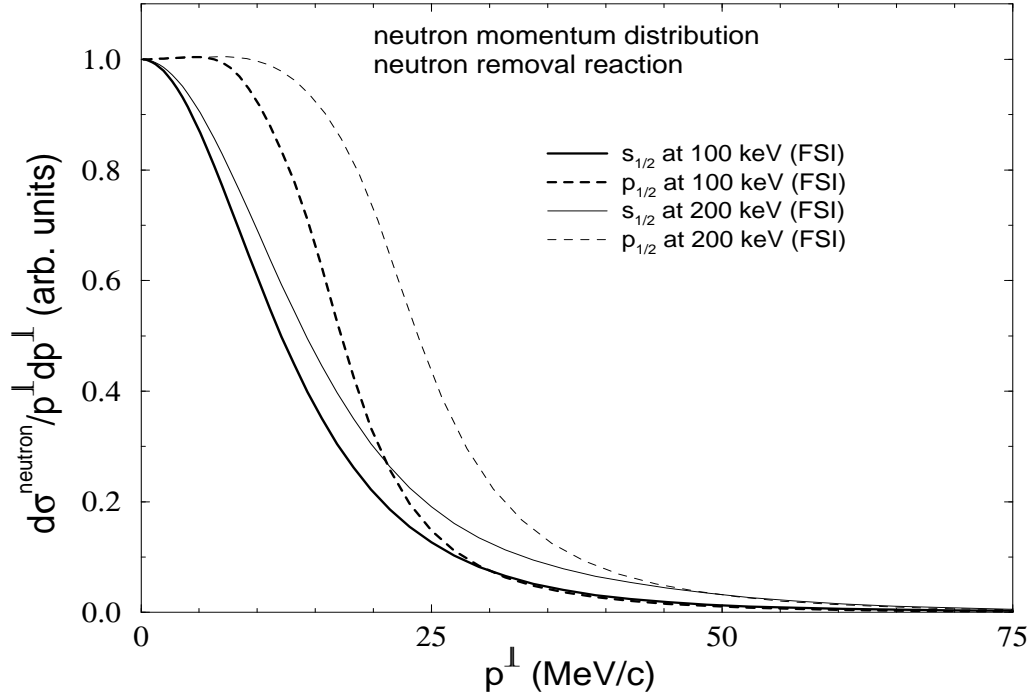

FIG. 3. Two-dimensional neutron momentum distribution for a neutron removal process in ^{11}Li fragmentation. FSI has been included in all the calculations. Solid curves represent the cases of low-lying virtual $s_{1/2}$-states at 100 keV (thick curve) and 200 keV (thin curve) in the neutron-^{9}Li subsystem. Dashed curves represent the case of low-lying $p_{1/2}$-resonances at 100 keV (thick curve) and 200 keV (thin curve) in the neutron-^{9}Li subsystem. The momentum of the neutron is referred to the center of mass of the ^{11}Li projectile. The ^{11}Li spin is assumed to be zero.

In fig.3 we show the two-dimensional neutron momentum distributions for a neutron removal process. The solid curves correspond to the cases where a virtual $s_{1/2}$-state is present at 100 keV (thick solid curve) and at 200 keV (thin solid curve) in the neutron-core subsystem, while the dashed curves represent the cases where a $p_{1/2}$-resonance is at 100 keV (thick dashed curve) and at 200 keV (thin dashed curve). In all these cases final state interactions have been included in the calculation.

For a neutron-core subsystem with a p-resonance at a given energy E_{res} the momentum distribution (with FSI)

will exhibit a peak at the relative neutron-core momentum $\mathbf{p}_r = \sqrt{\mu/m}\mathbf{k}_x = \sqrt{2\mu E_{\text{res}}/\hbar^2}$. For $E_{\text{res}} = 100$ keV and 200 keV, we then expect the peaks at $k_x \simeq 14$ MeV/c and at 19 MeV/c. In the two-dimensional neutron momentum distributions, we integrate away the dependence on $k_x^{\parallel}$ and refer to the center of mass of the projectile. Furthermore, even after including the s-wave contribution, which is 22% for the thick dashed curve and 36% for the thin dashed curve in fig.3, we still can see a clear bump in the momentum distributions corresponding to low-lying p-resonances. Thus, the effects of final state interactions on the two-dimensional neutron momentum distributions results in shapes, which depend very much on the structure of the low-lying state.
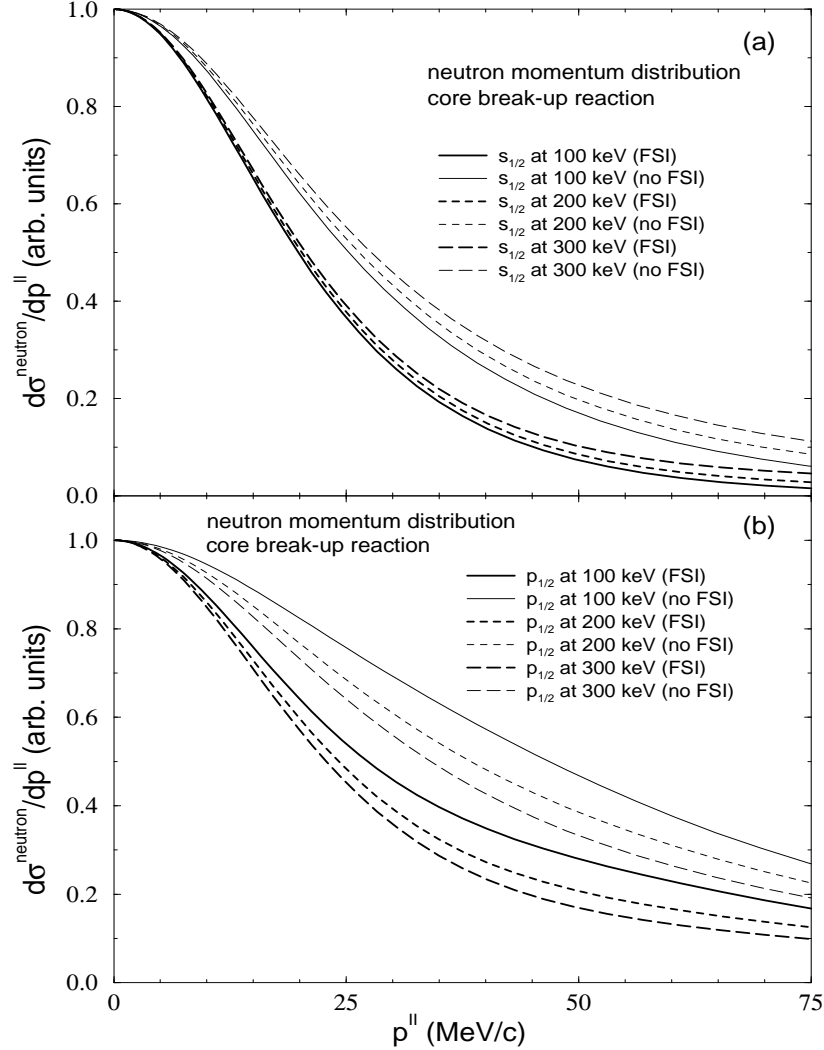
FIG. 4. The same as in fig.1 for one-dimensional neutron momentum distributions in a core break-up reaction.

Let us now turn to core break-up reactions, where the core is violently destroyed during the interaction, but where the sudden approximation still is valid. Then the final state interaction (neutron-neutron interaction) is well known and the uncertainties involved in the calculations are reduced. In fig.4 we show one-dimensional neutron momentum distributions for core break-up reactions. The FWHM for the curves in the figure is given in the fourth and sixth columns of table II, where the neutron momentum distributions without FSI are identical to those in fig.2.

We observe that the momentum distributions are rather insensitive to the structure of the neutron-core subsystem although the distributions are narrower for a higher s-wave content. This is due to the fact that the final state interaction (neutron-neutron interaction) is identical in all the cases and therefore independent of the characteristics of the neutron-core interaction. Thus, the momentum distributions are sensitive to the ^{10}Li structure only through the ^{11}Li wave function. On the other hand, the effect produced by the final state interaction is significant, especially for a low-lying $p_{1/2}$-resonance in ^{10}Li. Comparison with the experimental width for the neutron momentum distribution

in core break-up reactions again suggests a low-lying virtual s-state in ^{10}Li, see table II.

C. Momentum Distributions for Finite Core Spin

Up to now we have neglected the spin dependence of the neutron-core interaction or equivalently assumed that the spin of the core is zero. Any realistic calculation should of course assume that the spin of ^{9}Li is 3/2, and the neutron-core potential should include a spin dependence splitting the two s-states in ^{10}Li into states of total angular momenta 1 and 2. To do this, we have in the neutron-core potential included a term proportional to $\mathbf{s}_n \cdot \mathbf{s}_c$, where $\mathbf{s}_n$ is the spin of the neutron and $\mathbf{s}_c$ the spin of the core. For simplicity the spin splitting term has been introduced only in the s-wave, see eq.(40).

The V_s parameter has been chosen to be -7.14 MeV, the spin splitting parameter γ_s is taken as -0.13 for the solid curve and as 0.13 for the dashed curve. With these values the solid curves correspond to a situation where the lowest virtual s-state in ^{10}Li has spin 1 and an energy of 50 keV, while the second s-state has spin 2 and energy 340 keV. For the dashed curves the lowest virtual s-state in ^{10}Li has spin 2 and energy 97 keV, and the s-state with spin 1 has an energy of 460 keV. In both cases, the average position of the virtual s-states is about 230 keV. In these calculations we have taken $V_{l=1} = -19.14$ MeV and $V_{so} = 6.97$ MeV, placing the lowest p-resonance in ^{10}Li at 0.5 MeV. Final state interactions are included.
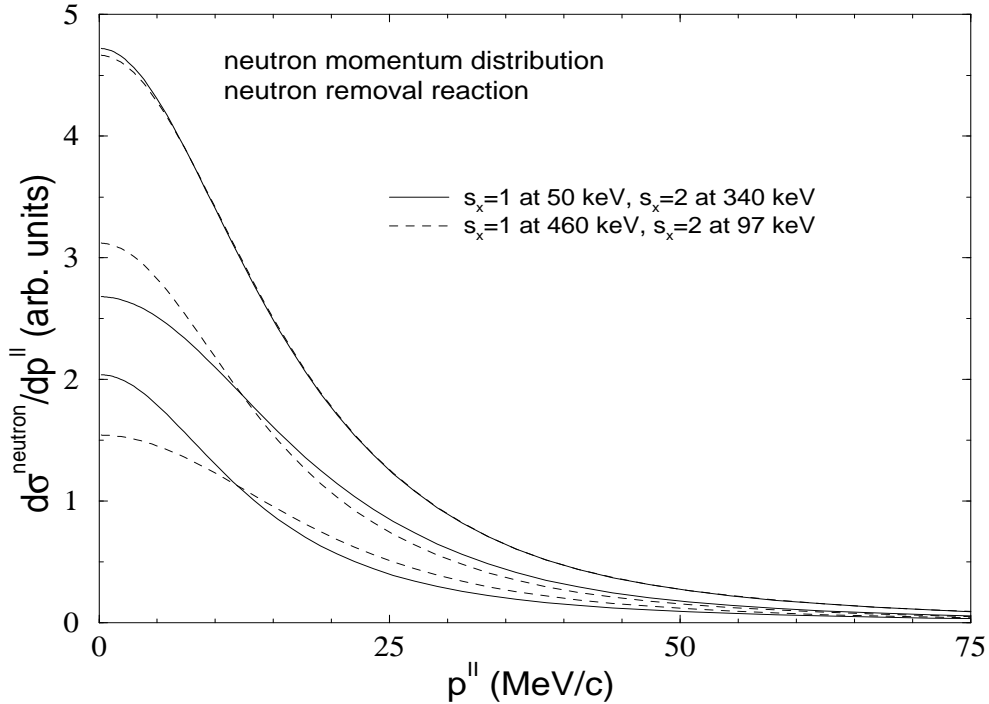

FIG. 5. One-dimensional neutron momentum distribution for a neutron removal process in ^{11}Li fragmentation. Solid curves: The virtual s-states in ^{10}Li are at 50 keV for $s_x = 1$ and at 340 keV for $s_x = 2$. Dashed curves: The virtual s-states in ^{10}Li are at 460 keV for $s_x = 1$ and at 97 keV for $s_x = 2$. For each case, the lower, the middle and the upper curves are obtained assuming that the spin of the final state system is 1, 2 and undefined, respectively.

The momentum distributions can now be divided into two parts arising respectively from angular momentum 1 and 2 of the final two-body state. This amounts to a separation of terms with $j_x = 1$ and 2 in eq.(33). In principle they can be measured independently. In fig.5 we plot results for the one-dimensional neutron momentum distribution for a neutron removal process. We have computed and plotted three curves for each case. The lowest curve (normalized to 3/8) is the one-dimensional neutron momentum distributions assuming that the final two-body system has spin 1. For the next curve (normalized to 5/8) the final two-body state is assumed to have spin 2. Finally the upper curve is the sum of the two others and therefore normalized to 1. For a final state of spin 1, the widths of the momentum distributions clearly increase with the energy of the virtual s-state. Compare the lowest solid and dashed curves

with FWHM of 26 and 37 MeV/c, respectively. This trend is also seen for a final state of spin 2. Compare here the intermediate solid and dashed curves with FWHM of 36 and 30 MeV/c, respectively.

We now assume that the spin of the two-body system in the final state is not measured. Then the distributions for the individual spins should be averaged with the statistical weighting already included in the normalizations. This amounts to include the s_x summation in eq.(33). The two cases in fig.5 resulting in the upper the solid and dashed curves can hardly be distinguished (FWHM=32 MeV/c). This is due to the fact that the statistically weighted average energy of the two virtual s-states in ^{10}Li in both cases is about 230 keV. The Pauli principle dictates that both s-states independent of splitting are equally occupied in ^{11}Li. The influence of the p-resonance at 0.5 MeV is insignificant and the s-wave content is always about 91%. Therefore the narrow distribution arising from one state must then be compensated by the broader distribution from the other s-state.

Thus, when the spin of the final two-body state is unknown the momentum distributions are only sensitive to the average position of the virtual s-states and the s-wave content in the initial wave function. Of course this conclusion also holds for core momentum distributions and core break-up reactions. If the momentum distributions could be measured for a given spin of the final two-body state, information about the lowest lying virtual s-state of ^{10}Li could be extracted from our analyses in a very direct way.

IV. REALISTIC CALCULATIONS FOR ^{11}LI

The calculations we made in the previous subsection, even though a very simple ^{11}Li structure was assumed, indicate that the unbound ^{10}Li nucleus has a low-lying virtual s-state (table II). A low lying p-resonance clearly overestimates both the width of the core momentum distribution and the neutron momentum distribution in a core break-up reaction. Recent analyses suggest that a virtual s-state is present at around 50 keV [14] together with a p-resonance at 0.5 MeV [30].

We first adjust the strength parameters in the neutron-^{9}Li potential, where $V_{l=1}$ and V_{so} are chosen to place the lowest p-resonance at 0.5 MeV. The spin-orbit parameter V_{so} is used to vary the p-wave content in the neutron-^{9}Li subsystem of the total ^{11}Li wave function. This is achieved by moving the higher-lying p-resonances up or down. Then the values of the parameters V_s and γ_s are chosen to give a low-lying virtual s-state and at the same time reproduce the correct binding energy and rms radius of ^{11}Li. The lowest virtual s-state in ^{10}Li is assumed to have spin 2, but choosing spin 1 instead does not produce significant changes of the numerical results. The interesting physical parameters are then energy and size of ^{11}Li, the p-wave content and the positions of the lowest s- and p-wave resonances in ^{10}Li.

In fig.6 we show one-dimensional ^{9}Li momentum distributions from ^{11}Li fragmentation. The energy of the lowest virtual s-state is 50 keV. Different p-state contents in the neutron-^{9}Li subsystem have been considered, 4% (solid curves), 18% (short-dashed curves), 26% (long-dashed curves), and 35% (dot-dashed curves). The thick and the thin curves are the calculations with and without final state interactions, respectively. The experimental data correspond to longitudinal ^{9}Li momentum distributions from a fragmentation process of a ^{11}Li projectile of energy 468 MeV/u and 648 MeV/u colliding with an Al target [31]. As expected and observed in fig.1, the effect of final state interactions is not very big, due to the large mass of the core. However, even these small effects seems to be necessary to reproduce the measured core momentum distributions, which in fact are rather insensitive to the structure of the neutron-core subsystem. All the curves including final state interactions match the experimental data equally well.

Deviations between measured and computed curves increase with momentum. Two different sources for this disagreement are obvious. First the three-body model does not include core degrees of freedom. Therefore, if the neutron-core distance is smaller than the core-radius of about 3 fm, or equivalently the neutron-core relative momentum is larger than about 65 MeV/c, the model is not applicable. Secondly, only contributions from nuclear break-up reactions are included in the sudden approximation and other processes are assumed to be negligible. This is in general believed to be very well fulfilled assumptions, especially for the longitudinal core momentum distributions considered here. A convincing example is the fragmentation of ^{6}He into an α-particle and a neutron, see [9]. Our case of ^{11}Li is expected to be more sensitive to possible additional contributions than this very well reproduced transverse momentum distribution of the α-particle. The good agreement for the major part of the momentum range in the fig.6 is an aposteriori confirmation of the validity of the model assumptions, i.e. the accuracy of the three-body wave function, the treatment of the reaction mechanism and the incorporation of final state interactions.
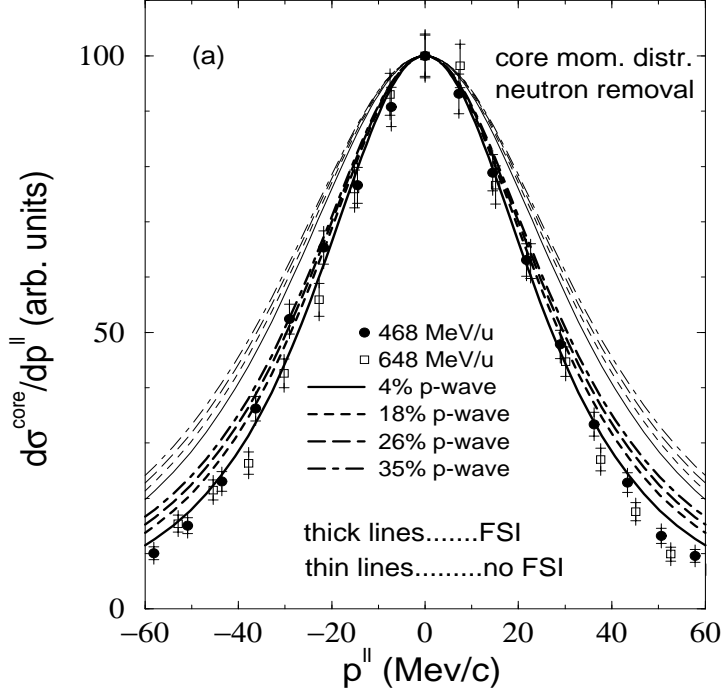
FIG. 6. One-dimensional core momentum distribution for a ^{11}Li fragmentation reaction. The lowest virtual s-state and p-resonance in ^{10}Li have an energy of 50 keV and 0.5 MeV, respectively. The thick (thin) curves are the calculations with (without) final state interactions. The p-wave content in the neutron-^{9}Li subsystem is 4% (solid curve), 18% (short-dashed curve), 26% (long-dashed curve), and 35% (dot-dashed curve). Experimental data are taken from [31].
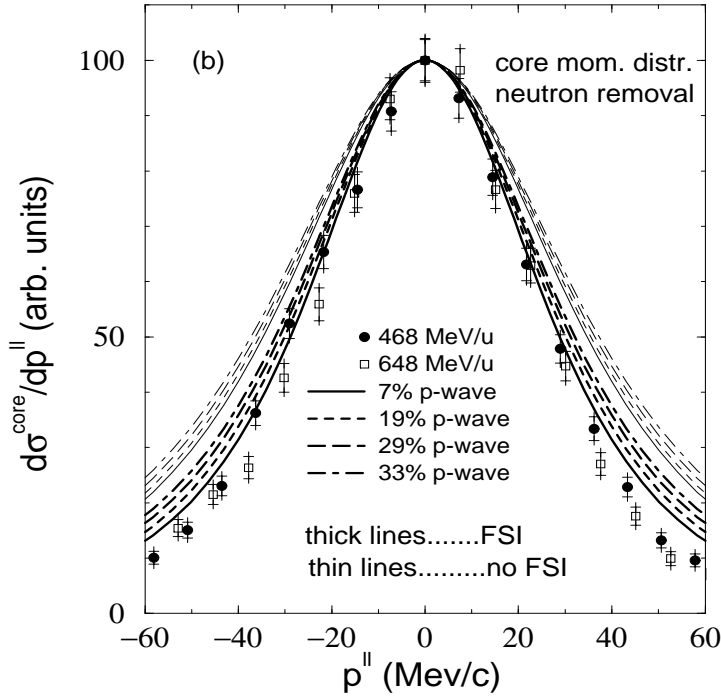

FIG. 7. Same as in fig.6 when the energy of the lowest virtual s-state in ^{10}Li is 200 keV. The p-wave content in the neutron-^{9}Li subsystem is 7% (solid curve), 19% (short-dashed curve), 29% (long-dashed curve), and 33% (dot-dashed curve).

When the energy of the lowest virtual s-state increases the core momentum distributions become broader as seen in fig.7, where the virtual s-state energy is 200 keV. The computed momentum distributions then overestimate the width of the experimental distributions, especially the ones with a higher p-wave content in the neutron-^{9}Li subsystem. This conclusion is perhaps only convincingly reached after both the visual impression from the figure and consultation of the numerical widths in table II. We can then consider 200 keV as an upper limit to the energy of the lowest virtual s-state. On the other hand, a lower limit to this energy is not provided by the core momentum distribution, which remains unchanged for virtual s-state energies below 50 keV.
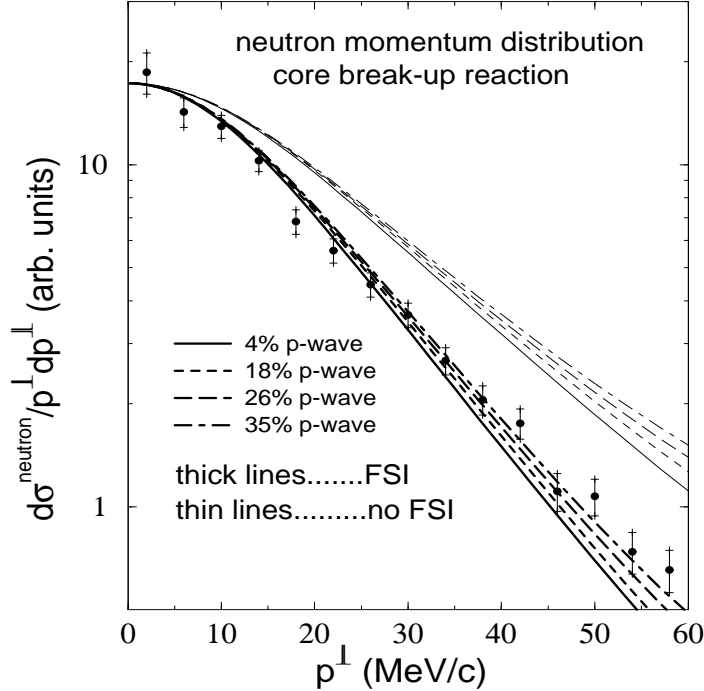

FIG. 8. Two-dimensional neutron core momentum distribution from a core break-up reaction. The lowest virtual s-state and p-resonance in ^{10}Li have an energy of 50 keV and 0.5 MeV, respectively. The interpretation of the curves is as in fig.6. Experimental data are taken from [15].

Let us focus now on neutron momentum distributions, where the effect of final state interactions is larger (figs.2, 3, and 4). Since for core break-up reactions the final state nucleon-nucleon interaction is well known, this kind of process is a good test for the model and the method of including final state interactions. In fig.8 we plot two-dimensional neutron momentum distributions for core break-up reactions for the same ^{10}Li structure as used in fig.6 (virtual s-state at 50 keV and p-resonance at 0.5 MeV). The meaning of the curves is also as described in fig.6. The experimental data are obtained in a fragmentation reaction with a C target and a ^{11}Li projectile of 280 MeV/u [15].

We observe that final state interactions now are crucial for reproducing the experimental distribution. The calculation with low p-wave content is too narrow, indicating that some p-state content is needed in the neutron-core subsystem. When we gradually increase the energy of the virtual s-state from 50 keV to 200 keV the momentum distributions remain esentially unchanged (the variations are of the size of the width of the curves). This insensitivity to the neutron-^{9}Li structure is not surprising, since the remaining particles (two neutrons) constitute a different subsystem.

Finally, we compute two-dimensional neutron momentum distributions for a neutron removal reaction. We first consider the case of a low-lying virtual s-state in ^{10}Li with an energy of 50 keV. The two-dimensional neutron momentum distributions are plotted in fig.9. The meaning of the curves is explained in fig.6. The experimental data are taken from a fragmentation reaction with a C target and a ^{11}Li projectile of 280 MeV/u [14]. We observe again that final state interactions are decisive in order to reproduce the experimental distribution. Since now the final state interaction depends on the details of the neutron-core potential, the computed distributions show a stronger dependence on the p-state content in the ^{10}Li subsystem. The momentum distribution with a low p-wave content underestimates the width of the distribution, while any neutron-core interaction producing more than 35% of p-wave content in ^{10}Li overestimates the width. The best agreement with the experimental distribution is found for a p-wave content ranging from 20 to 30%.
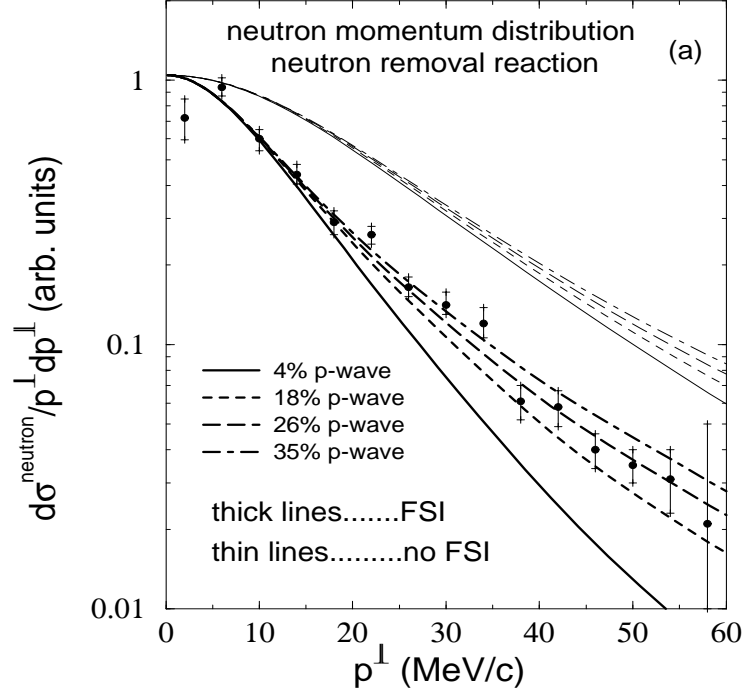
FIG. 9. Two-dimensional neutron core momentum distribution from a neutron removal reaction. The lowest virtual s-state and p-resonance in ^{10}Li have an energy of 50 keV and 0.5 MeV, respectively. The interpretation of the curves is as in fig.6. Experimental data are taken from [14].
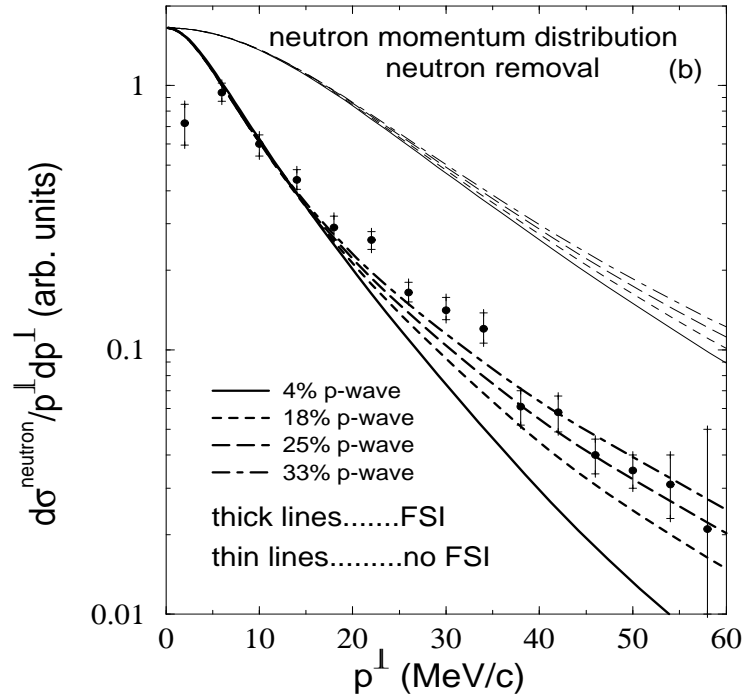

FIG. 10. Same as in fig.9 when the energy of the lowest virtual s-state in ^{10}Li is 10 keV. The p-wave content in the neutron-^{9}Li subsystem is 4% (solid curve), 18% (short-dashed curve), 25% (long-dashed curve), and 33% (dot-dashed curve).

17

Let us now investigate how these neutron momentum distributions are modified by a variation of the energy of the lowest virtual s-state in the neutron-core subsystem. In fig.10 we plot the same distributions as in fig.9 for a low-lying virtual s-state at 10 keV. The momentum distributions are now much steeper at low values of the momentum and the intermediate region is not well fitted. None of the distributions are able to reproduce the measured curve in the whole range of momenta. If we increase the p-wave content in the neutron-core subsystem to fit the intermediate region, we obtain too high values at large momenta. The best compromise would differ considerably more both at intermediate and high momenta than the compromise in fig.9. Furthermore, the deviation at very small momenta also seems to be larger although only based on essentially one measured point with fairly large error bars. Thus, we conclude that the virtual s-state energy in ^{10}Li must be larger than 10 keV.
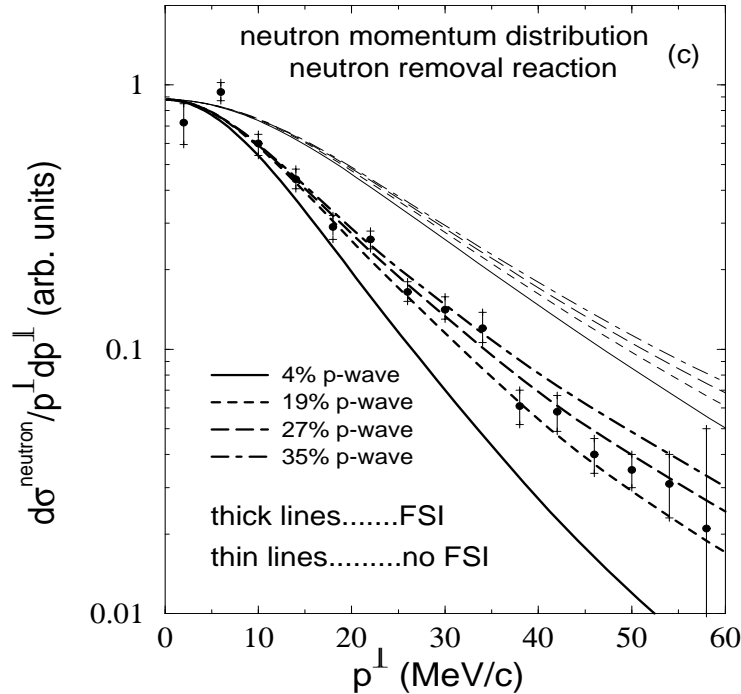

FIG. 11. Same as in fig.9 when the energy of the lowest virtual s-state in ^{10}Li is 100 keV. The p-wave content in the neutron-^{9}Li subsystem is 4% (solid curve), 19% (short-dashed curve), 27% (long-dashed curve), and 35% (dot-dashed curve).

For energies of the virtual s-state larger than 50 keV the experimental neutron distributions distributions are also reproduced fairly well. In fig.11 we show the same distributions as in figs.9 and 10, but for a virtual s-state energy at 100 keV. The agreement is improved from fig.10 and remains almost unchanged from fig.9. Even for higher virtual s-state energies the nice agreement is maintained. This is due to the lack of accurate experimental points at low momenta, which causes the uncertainty in the position of the origin of the distribution. A larger number of points in that region would further constrain the energy of the virtual s-state.

Comparing figs.9-11 we see that the best agreement with the experimental neutron momentum distributions is obtained for a p-wave content between 20 and 30%. The reason is that the behaviour of the distribution for large momenta is determined by the p-wave structure of the neutron-core subsystem. This structure is essentially the same in all these figures, i.e. the lowest p-resonance is placed at 0.5 MeV and the higher p-resonance considerably above. Furthermore, the neutron momentum distributions are rather insensitive to the position of the p-resonances. A very large variation of these energies are needed to change the shape of the distributions significantly at large momenta.

V. SUMMARY AND CONCLUSIONS

We have in this paper given a detailed formulation of a general method to describe fragmentation of high-energy three-body Borromean halo nuclei on light nuclear targets. In the previous papers in this series we established general properties of the structure of three-body halo nuclei. The most detailed information about these structures can be

obtained from measurements of momentum distributions of the fragments from reactions of halo nuclei with various targets. The inherent mixture of the initial halo structure and the reaction mechanism requires a description where both ingrediences are included. The present paper is devoted to construct a suitable method to study the properties of fragmentation products from halo nuclei.

The initial wave function must be available with a good precision and three-body computations are necessary. The reactions are described in the sudden approximation, where one of the particles instantaneously is removed from the three-body system while the other two particles are left undisturbed. This approximation is very well adapted for the weakly bound halo nuclei moving with high energy relative to the targets. The remaining two particles of the projectile move roughly in the beam direction while they continue to interact after the collision. This final state interaction is essential especially when low-lying resonances are present in the two-body system. The model must include these effects.

We use the recently developed method to solve the Faddeev equations in coordinate space. The initial three-body wave function is then accurately determined. We first briefly sketch this method, which is particularly well suited for an accurate treatment of the large-distance behavior. The low-energy scattering properties described by the scattering lengths are the decisive quantities determining the large-distance behavior of the three-body system. Therefore we parametrize the two-body interactions in terms of simple spin-dependent operators and gaussian radial shapes. We require that the relevant measured s- and p-wave scattering lengths as well as the singlet s-wave effective range are reproduced by the nucleon-nucleon interaction. The neutron-core interaction is adjusted to reproduce the size and binding energy of ^{11}Li and selected properties of ^{10}Li. The initial three-body wave function can now be accurately computed.

The halo nucleus reacts with a light target nucleus and one of the three particles is removed instantaneously. The final-state two-body wave function is asymptotically approaching the plane wave limit, but at smaller distances is influenced by the interaction between the remaining particles. We include this modification by a distorted wave approximation. This final-state two-body interaction is identically the same as the interaction entering in the computation of the initial three-body wave function. We maintain this consistency throughout the paper.

The model is now completely defined and we proceed to compute the transition matrix element which describes the probabilities for the various break-up processes. We integrate away analytically or numerically all non-observed quantities and end up with expressions for the observable momentum distributions of the remaining particles. Both one- and two-dimensional distributions are computed. To compare with the experimental results we tranform the particle momenta to the center of mass of the three-body halo nucleus. This is a straightforward but technically rather lengthy procedure.

Numerical results are presented to illustrate general aspects. We first assume a spin-less core and vary the s and p-state properties of the neutron-core system. The physical parameters are the energy of the lowest virtual s-state, the energy of the lowest p-resonance and the p-wave admixture in the neutron-core subsystem of the three-body wave function. The size and binding energy of the three-body system is left unchanged at values corresponding to ^{11}Li.

Three different momentum distributions can be calculated, i.e. (i) the core momentum distribution after neutron removal, (ii) the neutron momentum distribution after neutron removal and (iii) the neutron momentum distribution in a core break-up reaction. They each carry different information. For (i) the effects of final state interactions increase and the widths of the distributions decrease with increasing s-wave content of the neutron-core subsystem. The centrifugal barrier is crucial for this behavior. For (ii) the final state interaction is crucial and the momentum distributions strongly depend on the structure of the continuum spectrum of the neutron-core subsystem. The lower the virtual state or resonances the larger the effect. For (iii) the well known neutron-neutron final state interaction has a significant effect on the distributions while the properties of the neutron-core subsystem are less important.

The effects of finite core spin are necessary for realistic comparison with experimental data for halo nuclei. The resulting spin splitting of the lowest virtual s-states in the neutron-core system seems to produce quantitative and perhaps even qualitative differences. However, in most cases only the statistically weighted average energy is important due to the constraints from the Pauli principle, the parity conservation and the known energy of the three-body system. One exception occurs when the two-body final-state total angular momentum is measured in addition to the momentum distributions. Then the angular momentum of the relative state is determined and only one of the s-states contributes. The large difference, due to final state interactions, between the momentum distributions from the spin split states can in this way be observed.

Finally, we perform realistic calculations for ^{11}Li and compare with the avalaible experimental data. Since the final state neutron-neutron interaction is well known, core break-up reactions constitute a good test of the method used to incorporate final state interactions in the description of the process. The uncertainties involved in the calculation are therefore reduced. The other type of process, neutron removal reactions involve the structure of the unbound system ^{10}Li (^{9}Li +n), that simultaneously is crucial for the structure of the ^{11}Li three-body projectile.

The comparison with the experimental data permits us to conclude that the final state interaction is an essential ingredient in the computation of the momentum distributions, even for core momentum distributions. The p-wave

content in the neutron-^{9}Li subsystem has been concluded to be between 20% and 30%. From the longitudinal core momentum distribution and the radial neutron momentum distribution for a neutron removal process we conclude that the energy of the lowest virtual s-state in ^{10}Li must be between 30 keV and 200 keV. To improve the uncertainties in these conclusions, more accurate experimental data for neutron momentum distributions for low values of the momentum would be very helpful.

In conclusion, a consistent model has been developed to analyze momentum distributions of the particles after high-energy fragmentation reactions of three-body halo systems. Final state interactions are essential. Application to ^{11}Li and comparison with available data led to rather severe constraints on the properties of both ^{11}Li and the unbound ^{10}Li nucleus.

APPENDIX A: HYPERSPHERICAL AND HYPERANGULAR COORDINATES

We consider a system of three particles with masses m_i and coordinates $\mathbf{r}_i$ $(i = 1, 2, 3)$. The Jacobi coordinates are defined as

$$\mathbf{x}_k = a_{ij}(\mathbf{r}_i - \mathbf{r}_j) , \qquad \mathbf{y}_k = a_{(ij)k}\left(\frac{m_i\mathbf{r}_i + m_j\mathbf{r}_j}{m_i + m_j} - \mathbf{r}_k\right) ,$$
$$a_{ij} = \left(\frac{1}{m}\frac{m_i m_j}{m_i + m_j}\right)^{1/2} , \quad a_{(ij)k} = \left(\frac{1}{m}\frac{(m_i + m_j)m_k}{m_i + m_j + m_k}\right)^{1/2} , \tag{A1}$$

where $\{i, j, k\}$ is a cyclic permutation of $\{1, 2, 3\}$, and m is an arbitrary normalization mass.

From these definitions we find the momenta $\mathbf{k}_{xk}$ and $\mathbf{k}_{yk}$ to be:

$$\mathbf{k}_{xk} = \frac{1}{a_{ij}}\left(\frac{m_j}{m_i + m_j}\mathbf{p}_i - \frac{m_i}{m_i + m_j}\mathbf{p}_j\right) , \tag{A2}$$

$$\mathbf{k}_{yk} = \frac{1}{a_{(ij)k}}\left(\frac{m_k}{m_i + m_j + m_k}(\mathbf{p}_i + \mathbf{p}_j) - \frac{m_i + m_j}{m_i + m_j + m_k}\mathbf{p}_k\right) , \tag{A3}$$

where $\mathbf{p}_i$, $\mathbf{p}_j$, and $\mathbf{p}_k$ are the momenta of the three particles. When these momenta are referred to the center of mass of the three-body system $(\mathbf{p}_i + \mathbf{p}_j + \mathbf{p}_k = 0)$ we get

$$\mathbf{p}_i = a_{ij}\mathbf{k}_{xk} + \frac{m_i}{m_i + m_j}a_{(ij)k}\mathbf{k}_{yk} , \tag{A4}$$

$$\mathbf{p}_j = -a_{ij}\mathbf{k}_{xk} + \frac{m_j}{m_i + m_j}a_{(ij)k}\mathbf{k}_{yk} , \tag{A5}$$

$$\mathbf{p}_k = -(\mathbf{p}_i + \mathbf{p}_j) = -a_{(ij)k}\mathbf{k}_{yk} . \tag{A6}$$

The hyperspherical variables $\{\rho, \alpha_i, \Omega_{xi}, \Omega_{yi}\}$ are defined as

$$\rho = \sqrt{x_i^2 + y_i^2} , \qquad \alpha_i = \arctan(x_i/y_i) , \tag{A7}$$

where Ω_{xi} and Ω_{yi} define the directions of $\mathbf{x}_i$ and $\mathbf{y}_i$.

Analogously we define the hyperspherical variables in momentum space $\{\kappa, \alpha_{\kappa i}, \Omega_{k_x i}, \Omega_{k_y i}\}$ as

$$\kappa = \sqrt{k_{xi}^2 + k_{yi}^2} , \qquad \alpha_{\kappa i} = \arctan(k_{xi}/k_{yi}) , \tag{A8}$$

where $\Omega_{k_x i}$ and $\Omega_{k_y i}$ define the directions of $\mathbf{k}_{xi}$ and $\mathbf{k}_{yi}$.

[1] K. Riisager, A.S. Jensen, and P. Møller, Nucl. Phys. **A548**, 393 (1992).

[2] D.V. Fedorov, A.S. Jensen, and K. Riisager, Phys. Lett. **B312**, 1 (1993).

[3] D.V. Fedorov, A.S. Jensen, and K. Riisager, Phys. Rev. **C49**, 201 (1994).

[4] D.V. Fedorov, A.S. Jensen, and K. Riisager, Phys. Rev. **C50**, 2372 (1994).

[5] P.G. Hansen, A.S. Jensen, and B. Jonson, Annu. Rev. Nucl. Part. Sci. 45, 591 (1995).

[6] C. Detraz and D.J. Vieira, Annu. Rev. Nucl. Part. Sci. 39, 407 (1989).

[7] P.G. Hansen and B. Jonson, Europhys. Lett. **4**, 409 (1987).

[8] L. Johannsen, A.S. Jensen, and P.G. Hansen, Phys. Lett. **B244**, 357 (1990).

[9] M.V. Zhukov, B.V. Danilin, D.V. Fedorov, J.M. Bang, I.J. Thompson, and J.S. Vaagen, Phys. Rep. **231**, 151 (1993).

[10] T. Kobayashi, O. Yamakawa, K. Omata, K. Sugimoto, T. Shimoda, N. Takahashi and Tanihata, Phys. Rev. Lett. **60**, 2599 (1988).

[11] R. Anne *et al.*, Phys. Lett. **B250**, 19 (1990).

[12] N.A. Orr *et al.*, Phys. Rev. Lett. **69**, 2050 (1992).

[13] N.A. Orr *et al.*, Phys. Rev. **C51** 3116 (1995).

[14] M. Zinser *et al.*, Phys. Rev. Lett. **75**, 1719 (1995).

[15] T. Nilsson *et al.*, Europhys. Lett. **30**, 19 (1995)

[16] F. Humbert *et al.*, Phys. Lett. **B347**, 198 (1995).

[17] M.V. Zhukov, L.V.Chulkov, D.V. Fedorov, B.V. Danilin, J.M. Bang, J.S. Vaagen and I.J. Thompson, J. Phys. **G20**, 201 (1994).

[18] A.A. Korsheninnikov and T. Kobayashi, Nucl. Phys. **A567**, 97 (1994).

[19] M.V. Zhukov and B. Jonson, Nucl. Phys. **A589**, 1 (1995).

[20] F. Barranco, E. Vigezzi, and R.A. Broglia, Phys. Lett. **B319**, 387 (1993).

[21] D.V. Fedorov, E. Garrido, and A.S. Jensen, Phys. Rev. **C51**, 3052 (1995).

[22] E. Garrido, D.V. Fedorov and A.S. Jensen, Phys. Rev. **C**, (1996), in press.

[23] J.M. Bang and I.J. Thompson, Phys. Lett. **B279**, 201 (1992).

[24] I.J. Thompson and M.V. Zhukov, Phys. Rev. **C49**, 1904 (1994).

[25] R.G. Newton, Scattering Theory of Waves and Particles, (Springer-Verlag, N.Y., 1982), Second Edition, p.444.

[26] D.M. Brink and G.R. Satchler, Angular Momentum, (Oxford University Press, London, 1962).

[27] O. Dumbrajs, R. Koch, H. Pilkuhn, G.C. Oades, H. Behrens, J.J. de Swart, P. Kroll, Nucl. Phys. **B216**, 227 (1983).

[28] B.M. Young *et al.*, Phys. Rev. Lett. **71**, 4124 (1993).

[29] I. Tanihata *et al.*, Phys. Lett. **B287**, 307 (1992).

[30] B.M. Young *et al.*, Phys. Rev. **C49**, 279 (1994).

[31] H. Geissel and W. Schwab, private communication.